W. G. Li

X. Y. Luo[1]

N. A. Hill

School of Mathematics and Statistics,
University of Glasgow,
Glasgow, G12 8QW, UK

R. W. Ogden

School of Mathematics and Statistics,
University of Glasgow,
Glasgow, G12 8QW, UK;
School of Engineering,
University of Aberdeen,
Aberdeen, AB24 3UE, UK

A. Smythe

A. W. Majeed

N. Bird

Academic Surgical Unit,
Royal Hallamshire Hospital,
Sheffield, S10 2JF, UK

A Quasi-Nonlinear Analysis of the Anisotropic Behaviour of Human Gallbladder Wall

Estimation of biomechanical parameters of soft tissues from noninvasive measurements has clinical significance in patient-specific modeling and disease diagnosis. In this work, we present a quasi-nonlinear method that is used to estimate the elastic moduli of the human gallbladder wall. A forward approach based on a transversely isotropic membrane material model is used, and an inverse iteration is carried out to determine the elastic moduli in the circumferential and longitudinal directions between two successive ultrasound images of gallbladder. The results demonstrate that the human gallbladder behaves in an anisotropic manner, and constitutive models need to incorporate this. The estimated moduli are also nonlinear and patient dependent. Importantly, the peak stress predicted here differs from the earlier estimate from linear membrane theory. As the peak stress inside the gallbladder wall has been found to strongly correlate with acalculous gallbladder pain, reliable mechanical modeling for gallbladder tissue is crucial if this information is to be used in clinical diagnosis. [DOI: 10.1115/1.4007633]

Keywords: gallbladder, emptying, strain energy function, nonlinear analysis, constitutive equation

1 Introduction

Gallbladder (GB) disease is a common condition that affects both women and men. Symptoms vary widely from mild discomfort to severe pain. In severe cases, the patient can suffer from jaundice, nausea, and fever. When this happens, GB removal (cholestectomy) usually by keyhole surgery, is normally recommended. In the UK, 50,000 cholecystectomies are performed each year; it is the most common elective abdominal operation performed in the NHS. The fundamental issue of understanding the underlying mechanisms of GB disease is therefore very important in terms of patient care provision and cost.

Histological studies by Caldwell Jr. et al. [1] delineate a three-layer structure in the wall of the GB of a mammalian species, the sea cow. The mucosal layer consists of columnar epithelium with lamina propria and has folds projecting into the GB lumen. The perimuscular layer is covered by serous mesothelium. The muscular layer consists of enormous bundles of smooth muscle cells oriented circumferentially and longitudinally. This layer is responsible for passive and active stress development. Electron microscopy of a transverse longitudinal section of a GB wall presents two large smooth muscle bundles running almost orthogonal to each other in the muscle layer. During stimulation with CCK (Cholecystokinin-8), a peptide hormone that stimulates the gall bladder muscle to contract and release bile from the lumen, strips from human GB wall in the circumferential direction demonstrated a slightly stiffer response than in the longitudinal direction [2]. Additionally, passive tensile tests for human GB primarily disclose different Young's moduli in the strips isolated from the body of sample GBs in circumferential and longitudinal orientations [3]. This evidence suggests that the GB wall has an anisotropic structure. In addition, studies on guinea-pigs of the

mechanical properties of the GB suggest that nonlinear effects are significant in the GB wall [4]. However, most of the modeling studies have accounted for the anisotropic and/or nonlinear behavior of the human GB wall [5–8].

A particular challenge in human GB modeling is the estimation of the patient-specific material properties. As in many other applications, human tissue mechanical elasticity can be used to indicate pathological changes caused by disease, e.g., carcinoma of the breast (Tilleman et al. [9]), plaque (Schulze-Bauer and Holzapfel [10]; Karimi et al.[11]) and aging problems (Escoffier et al. [12]; Lee et al.[13]); furthermore, it has the potential to be applied in clinical diagnoses [14]. How to evaluate mechanical properties of bio-tissue from medical images—a process termed elastography—is becoming an increasingly researched topic.

In elastography, one solves an inverse problem in which boundary conditions, load and strain or displacement field are known, but the stress-free configuration and mechanical properties are to be determined. This is in contrast to a direct problem, where the mechanical properties, boundary conditions, load and stress-free configurations are known and one solves for the strain or displacement. There is a different type of inverse problem, known as elastostatics, where one seeks the stress free configuration with the known mechanical properties, strain or displacement field, boundary conditions and loading [15–22]. In this work, we are only concerned with elastography.

In elastography, one estimates either the elastic moduli [23], or a general linear elasticity tensor [24] directly by solving the equilibrium equations in an iterative manner. Normally this requires solving direct linear problems repeatedly with successively updated material property constants. The computed strain or displacement field is then matched to experimental observations (or medical images). The process will be terminated when the difference of the estimated quantities between simulations and observations reach a minimum [11,14,25–33].

In the present paper, we use a quasi-linear elastography inverse approach to estimate GB tissue elasticity. Namely, we conduct the linear analyses on a series of configurations of human GBs determined by ultrasonographic routine scans during emptying [6,34].

[1]Corresponding author.

The transmural pressure in GBs, which was estimated from measured volume changes [6], is applied as the loading condition. The mechanical property constants are determined so that the computed displacements at several observation points are adjusted against those from clinical measurements with the errors minimized in the least-squares sense. This analysis leads to strain-dependent incremental Young's moduli of the GB tissue that can be used effectively to study the nonlinear anisotropic behavior of human GB during emptying.

2 The Computational Model

2.1 The Finite Element Model of GB. During the emptying under intravenous infusion of CCK (0.05 μg/kg body weight) [34], GB geometries were measured using ultrasound. Following Li et al. [7], we generate ellipsoidal membrane models from these images. These ellipsoids have the axes of lengths denoted by D_1, D_2, D_3 and a uniform thickness of h (Fig. 1). The transmural pressure of the GB can be estimated from a 1D Windkessel model [6]:

$$p = p_d + (p_e - p_d)\exp[(t_e - t)/RC] \tag{1}$$

where p_e and p_d are the mean pressures in the GB and duodenum at the end of emptying, t_e is the total time takes to empty the bile, C (the ratio of incremental volume over incremental pressure) is the compliance of the GB, and R is the flow resistance when the bile streams into the cystic and common bile ducts [6].

The forward problem is solved using the finite element analysis package ADINA 8.7.2. Although the material of the human GB wall is nonlinear, we assume the material parameters are constant
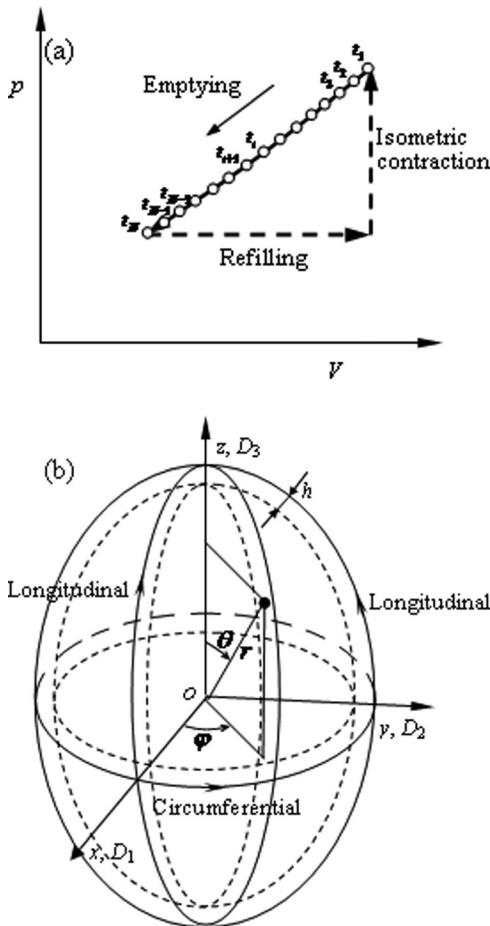

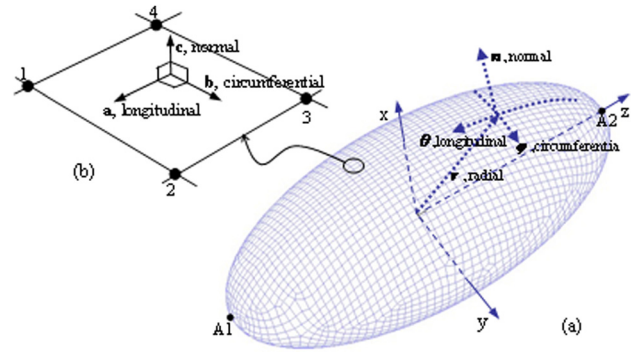**Fig. 1** (*a*) **The pressure-volume (*p–V*) diagram, and (*b*) the ellipsoid model of GB**

Fig. 2 A typical GB mesh and a 4-node membrane element showing the material local Cartesian system (*a*), (*b*), (*c*). φ, θ, and *n* are the spherical coordinates of GB model with the origin O (see Fig. 1). In the simulations, we choose these two coordinate systems to be the same. The boundary conditions are applied at the two apexes A1 and A2, see text for details.

between each increment of pressure loading. In a typical 4-node membrane element, the definitions of an orthotropic membrane and local material Cartesian coordinates are shown in Fig. 2. We use a spherical coordinate system (θ, φ, r) with the origin O for the GB geometry, as shown in Fig. 1(*b*), and choose the material coordinates (**a**, **b**, **c**) that are located on the mid-surface of a GB to be in the local θ (longitudinal), φ (circumferential), and n (normal) directions.

The constitutive relation for an orthotropic membrane is

$$
\begin{bmatrix} e_\theta \\ e_\varphi \\ e_n \\ \gamma_{\theta\varphi} \\ \gamma_{\theta n} \\ \gamma_{\varphi n} \end{bmatrix}
=
\begin{bmatrix}
1/E_\theta & -v_{\theta\varphi}/E_\varphi & -v_{\theta n}/E_n & 0 & 0 & 0 \\
-v_{\varphi\theta}/E_\theta & 1/E_\varphi & -v_{\varphi n}/E_n & 0 & 0 & 0 \\
-v_{n\theta}/E_\theta & -v_{n\varphi}/E_\varphi & 1/E_n & 0 & 0 & 0 \\
0 & 0 & 0 & 1/G_{\theta\varphi} & 0 & 0 \\
0 & 0 & 0 & 0 & 1/G_{\theta n} & 0 \\
0 & 0 & 0 & 0 & 0 & 1/G_{\varphi n}
\end{bmatrix}
\times
\begin{bmatrix} \sigma_\theta \\ \sigma_\varphi \\ 0 \\ \tau_{\theta\varphi} \\ 0 \\ 0 \end{bmatrix}
\tag{2}
$$

where $\nu_{kl}(k, l = \theta, \phi, n)$ are the Poisson's ratios, e_k, σ_k ($k = \theta$, φ, n) are the normal strains and stresses, respectively, γ_{kl}, τ_{kl} are the shear strains and stresses, respectively, and E_k, G_{kl} are the elastic Young's moduli and shear moduli, respectively. We further assume that the wall material of GB is transversely isotropic, that is

$$\nu_{\theta\varphi} = \nu_{\varphi n} = \nu, \quad E_\varphi = E_n, \quad G_{\theta n} = G_{\varphi n},$$
$$G_{\theta\varphi} = \frac{E_\theta}{2(1+\nu)}, \quad \text{and} \quad G_{\varphi n} = \frac{E_\varphi}{2(1+\nu)} \tag{3}$$

A finite element mesh for the GB is shown in Fig. 2. Mesh independence is checked first. When the maximum mesh size (edge length) is decreased from 2 mm to 1 mm, the maximum first principal stress only increases by 0.4%. We therefore used 1 mm as the maximum edge length for all meshes.

The Dirichlet boundary condition is applied at the two apexes of the GB, denoted as A1, A2 in Fig. 2(*a*). Specifically, all the
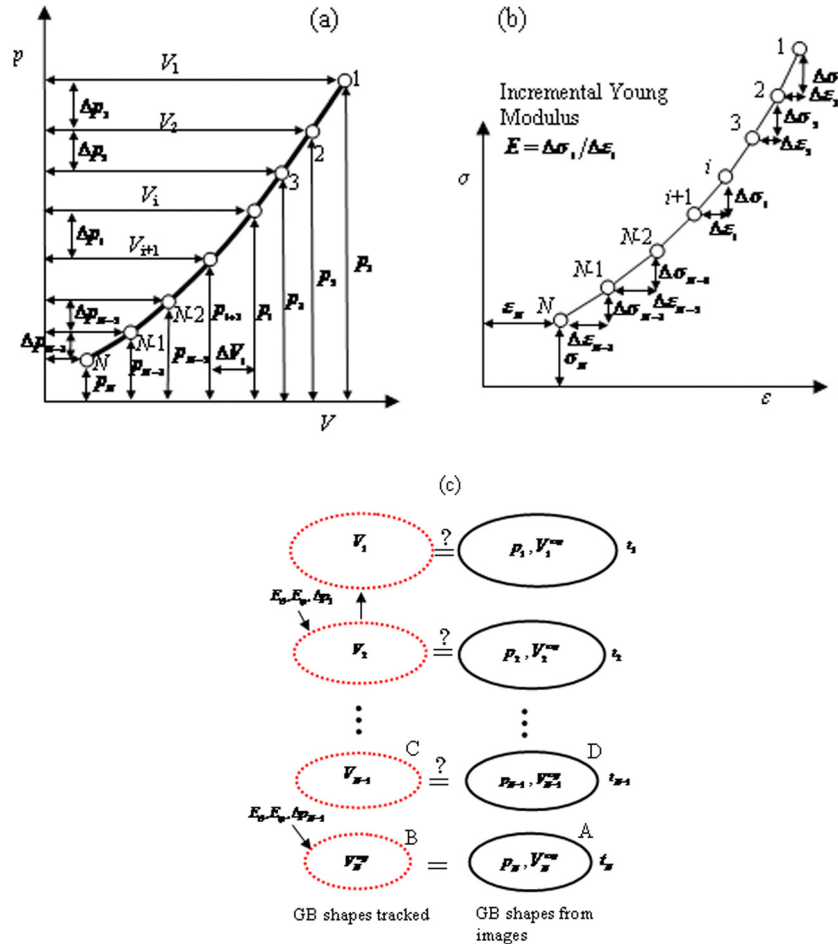
Fig. 3 Illustration of the incremental approach, with the computations starting from the initial configuration B at the end of emptying, and proceeding to the beginning of the emptying. (*a*) Incremental pressure loading and volume, (*b*) incremental stress and strain, and (*c*) sketch of the computational procedure. *V* and *V*^exp are the estimated and measured GB volumes, respectively.

displacements are fixed at A1, and only the displacements in the *x* and *y*-directions are fixed at A2.

2.2 The Incremental Approach. The incremental approach is carried out as a series of linear analyses between two successive image configurations, working backwards in the time from the end to the beginning of GB emptying phase. The GB wall material properties are assumed to be constant in each analysis, and the incremental pressure loadings are defined as (see Fig. 3(*a*)),

$$\Delta p_i = p_i - p_{i+1} \qquad (4)$$

where $i = N-1$, $N-2,\ldots$, 3, 2, 1, and N is the total number of images. $i = 1$ and N indicate the beginning and the end of emptying, respectively. The incremental stress and strain between two configurations i and $i+1$ (see Fig. 3(*b*)) are used to obtain the local incremental Young's modulus. The total stress and strain at the ith configuration are then
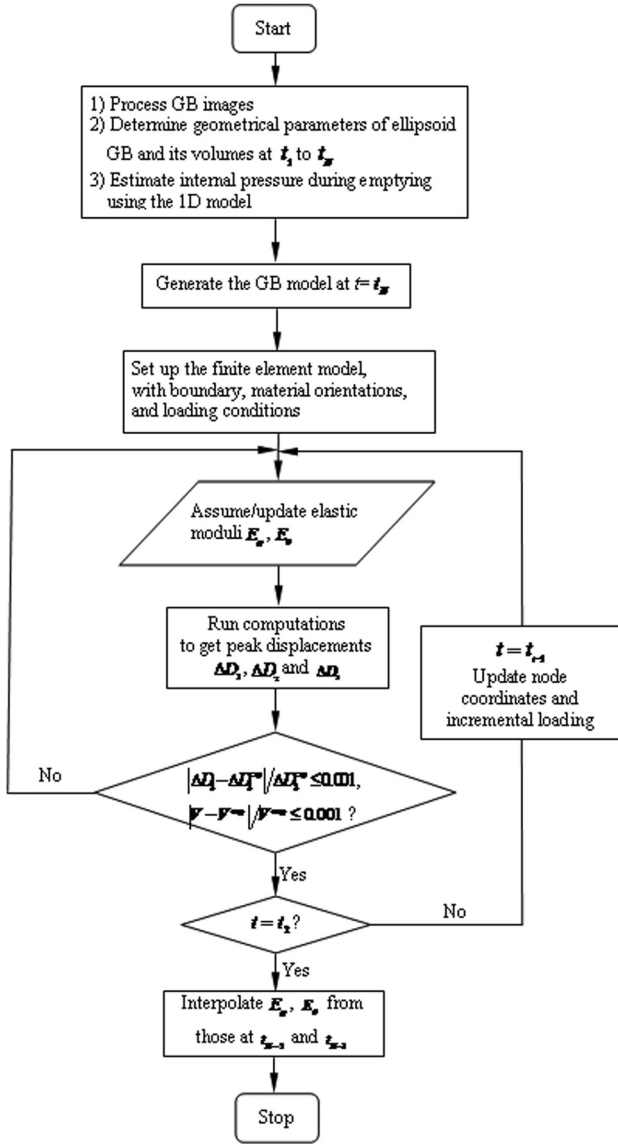
$$\sigma_i = \sigma_N + \sum_{k=i}^{N-1} \Delta\sigma_k$$

$$\varepsilon_i = \varepsilon_N + \sum_{k=i}^{N-1} \Delta\varepsilon_k \qquad (5)$$

Note that σ_N and ε_N are the initial stress and strain at the end of emptying (when $p_N = p_e$). The value of the intraluminal pressure

p_e is estimated to be around 11 mmHg [6], corresponding to a volume ejection fraction of 70% at the end of the emptying. The value of σ_N is then estimated from p_e using the linear membrane model of Li et al. [7,8]. As we do not know the constitutive relation between σ_N and ε_N, we assume that $\varepsilon_N = 0$. This assumption should have minor effect since the muscle at the end of emptying is relaxed, so deformation, if any, should be very small.

We start the computation from the configuration B at $t = t_N$ in Fig. 3(*c*), where B is assumed to be the same as the measured GB shape at configuration A, and perform a linear finite element analysis with an assumed set of elastic moduli and the incremental pressure loading of Δp_{N-1}. This gives us the deformed configuration C. We then compare C with the measured GB shape at configuration D. If the error between the shapes and volume of the two configurations is below a set tolerance, the procedure will be terminated and the assumed moduli are deemed to be correct. Otherwise the elastic moduli are updated iteratively using a bisection method until the requirement is satisfied. Normally, 5 to10 iterations are required to achieve the convergence tolerance of 10^{-3}. This process is repeated for all the time intervals on an updated mesh, until $t = t_1$. The material parameters at the initial time instance t_N are interpolated from those at the time step t_{N-2} and t_{N-1}. The detailed procedure is shown in Fig. 4.

Notice that in our computations an incremental pressure is applied to the GB configurations updated at t_{N-1}, $t_{N-2},\ldots$, t_3, t_2, respectively, based on the deformed mesh, and the incremental elastic moduli, as defined in Bergel [35], are estimated at each
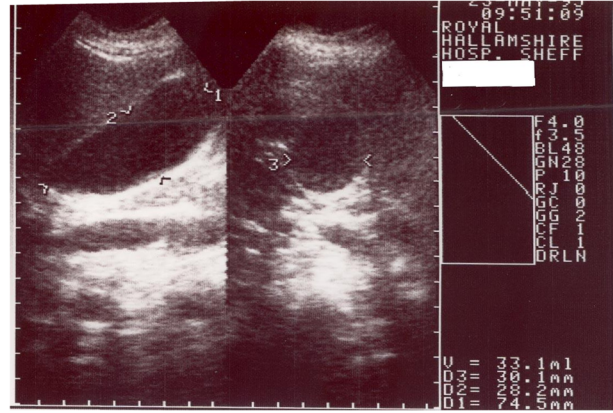
Fig. 5 The ultrasound image of GB-E (see Table 2) at the beginning of the emptying, in which the three axes D_1, D_2, and D_3 are shown. These are used to provide the comparison for the inverse approach, and the computed ellipsoid has the same axes within 0.1% error tolerance in D_3 and the volume.

Fig. 4 Flow chart for the inverse estimation of the elastic moduli, where ΔD_i and ΔD_i^{exp} ($i = 1, 2, 3$), are the estimated and measured maximal displacements along the three axes of ellipsoid, respectively. Note only V and ΔD_3 are used in the error control.

Table 1   Parameter values of six human GB samples

| Item | Parameter | Model GB No. | | | | | |
		A	B	C	D	E	F
Beginning of emptying	t_1(min)	0.0	0.0	0.0	0.0	0.0	0.0
	p_1(Pa)	2032.8	2206.5	3512.4	2377.7	2598.1	2361.9
	D_1^1(mm)	23.4	27.2	34.7	24.1	28.2	30.5
	D_2^1(mm)	25.0	27.2	35.7	30.8	30.1	30.5
	D_3^1(mm)	54.1	55.9	92.3	68.6	74.5	53.8
End of emptying	t_N(min)	615.3	80.4	55.3	18.2	32.9	105.4
	$p_N = p_e$(Pa)	1466.5	1466.5	1466.5	1466.5	1466.5	1466.5
	D_1^N(mm)	14.2	18.0	22.6	17.1	17.5	19.1
	D_2^N(mm)	15.4	17.5	24.7	18.5	20.4	22.7
	D_3^N(mm)	43.6	39.4	61.4	48.3	53.1	34.7
Clinical criterion	EF at $t = 30$ min	Very poor	Poor	Good	Excellent	Good	Poor

time step t_i ($i = N–1$, $N–2$, …, 2, 1). This gives rise to a quasi-linear stress-strain (σ-ε) relation, as shown in Fig. 3(b).

3 Results

3.1 GB Samples. Six GB samples, namely GB-A to GB-F, chosen from the GB samples 1, 17, 19, 21, 30, and 37 in a previous study [7], are selected for the study. These GBs differ from each other in size and emptying behavior; a typical ultrasound image is shown in Fig. 5. The parameters are listed in detail in Table 1. In all computations, we assume that $h = 2.5$ mm, $p_e = 11$ mmHg, $p_d = 6$ mmHg, and $C = 2.73$ mL/mmHg [6,7]. An example of the finite element mesh for a GB model is shown in Fig. 2. In all computations we also set $N = 15$, which ensures that the incremental peak strain at each step is less than 4%.

3.2 Estimated Elastic Moduli. Figure 6 shows the longitudinal, E_θ, and circumferential, E_φ, elastic moduli, and their ratio for all six GB models. It is clear that the estimated elastic moduli increase almost linearly with the GB volume. In other words, GBs stiffen when they are stretched. This agrees with the behavior of other soft bio-tissues [36,37]. Furthermore, the ratio of elastic moduli, E_φ/E_θ, is greater than unity, implying that the human GB wall is strongly anisotropic. In particular, GB-C has the most slender geometry with the smallest initial diameter ratios (D_1^1/D_3^1, D_2^1/D_3^1), and it presents the strongest anisotropic behavior (the largest value of E_φ/E_θ).

The computed peak principal stresses σ_1, $\sigma_2(= \sigma_\theta, \sigma_\varphi)$ are plotted against the corresponding principal cumulative strains ε_1, $\varepsilon_2(= \varepsilon_\theta, \varepsilon_\varphi)$ in Fig. 7. To facilitate comparisons with other published work (see the Discussion), we note that the stress-strain curves can be fitted well with exponential functions

$$\sigma_i = \alpha_i \exp(\gamma_i \varepsilon_i), i = 1, 2 \qquad (6)$$

where α_i, γ_i are the fitting parameters listed in Table 2.
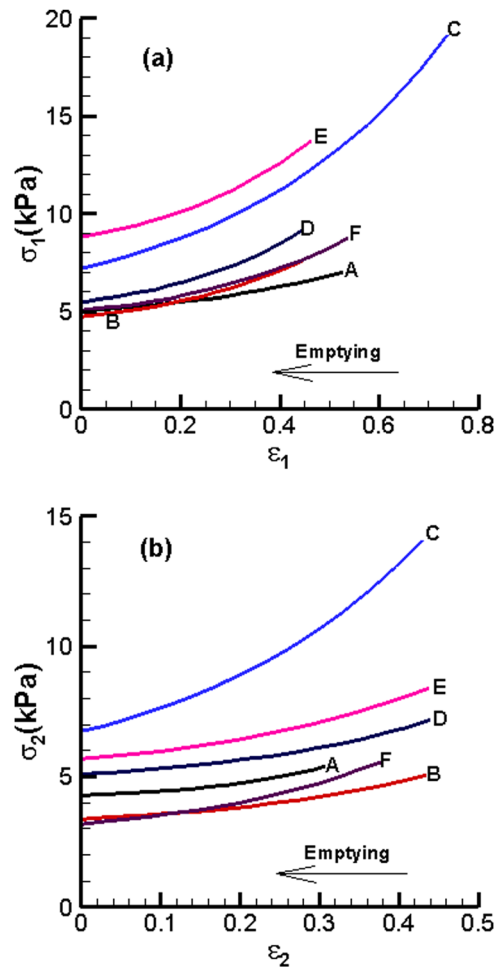
3.3 Peak Displacements, Volume, and Stress Patterns. A comparison of the peak displacements between the images and computed GBs is shown in Fig. 8. An overall good agreement between the computed and measured geometries is achieved for most of the GB samples. The only obvious discrepancy is observed for GB-D in the short axes (ΔD_1 and ΔD_2). This is because for most of the GB samples, the deformed cross-sectional area remains more or less circular, i.e., they are more like an ellipsoid of revolution ($D_1 \approx D_2 < D_3$). This behavior can be better
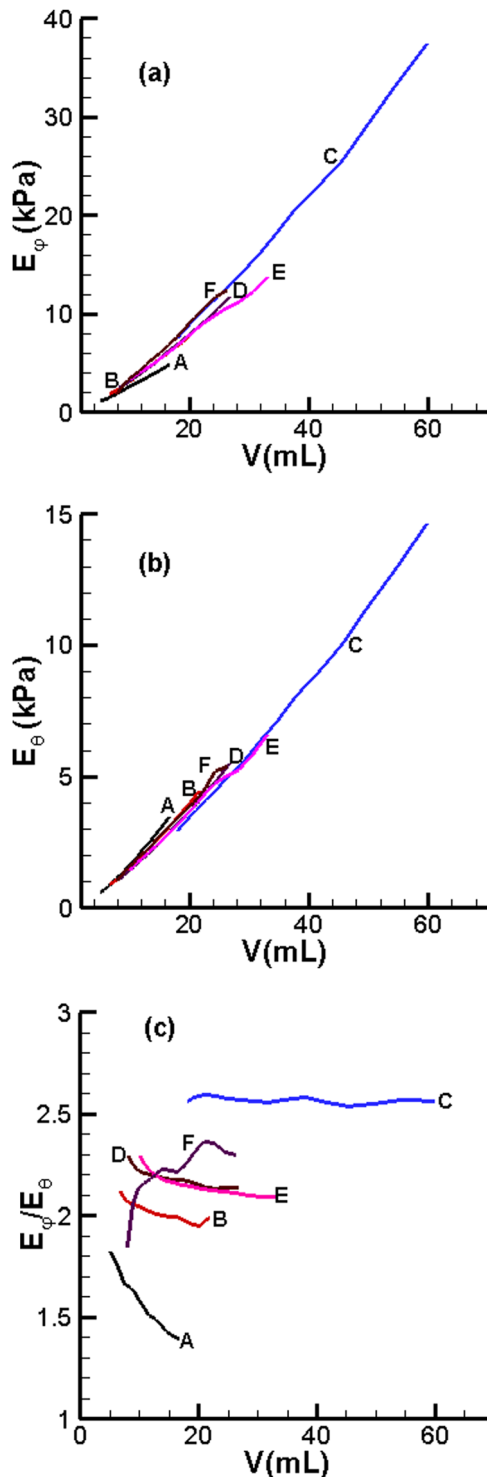
Fig. 6 Values of elastic moduli in the circumferential and longitudinal directions and their ratios for the six GB samples: (a) E_φ, (b) E_θ, and (c) E_φ/E_θ

Fig. 7 Values of the peak principal stresses σ_1, σ_2 versus corresponding cumulative principal strains ε_1, ε_2 of the six GB models: (a) $\sigma_1 - \varepsilon_1$, (b) $\sigma_2 - \varepsilon_2$. Note that GB-C, GB-D, and GB-E have higher stress curves than the others, especially in the first principal direction.

Table 2 Estimated parameters for Eq. (6)

				Model no.			
Curve	Parameter	GB-A	GB-B	GB-C	GB-D	GB-E	GB-F
$\sigma_1 - \varepsilon_1$	α_1(kPa)	4.9107	4.5685	6.8065	5.2348	8.4885	4.8119
	γ_1	0.6233	1.0573	1.3267	1.1649	0.9636	1.0314
$\sigma_2 - \varepsilon_2$	α_2(kPa)	4.1447	3.2403	6.4665	4.9155	5.4929	3.0737
	γ_2	0.7497	0.9342	1.7121	0.7772	0.8898	1.4573

described by our transversely isotropic membrane model. However, GB-D deforms with an ellipsoidal cross-sectional shape, and hence is not transversely isotropic.

A detailed stress pattern for GB-F at the beginning of the emptying is shown in Fig. 9. This is compared with the results using the linear membrane model [7]. We remark that the present results have similar stress patterns to those from the linear membrane models; although the maximum peak stress obtained using the present approach is somewhat different from that of the linear

membrane model, the overall trend is similar—a summary of the peak principal stresses is shown in Table 3. The poorest comparison is for GB-D where the GB shape cannot be tracked accurately by this model (see Fig. 7, GB-D). This is discussed later.

4 Discussion

We have performed an incremental method to determine the elastic moduli of human GB wall using in vivo images and estimates for the peak pressure at the beginning of the emptying. As measuring patient-specific pressure noninvasively is not practical clinically, we have estimated the peak pressure from a Windkessel model [6], in which a mean compliance is assumed for all GB samples. In the following, we provide our best estimate of the
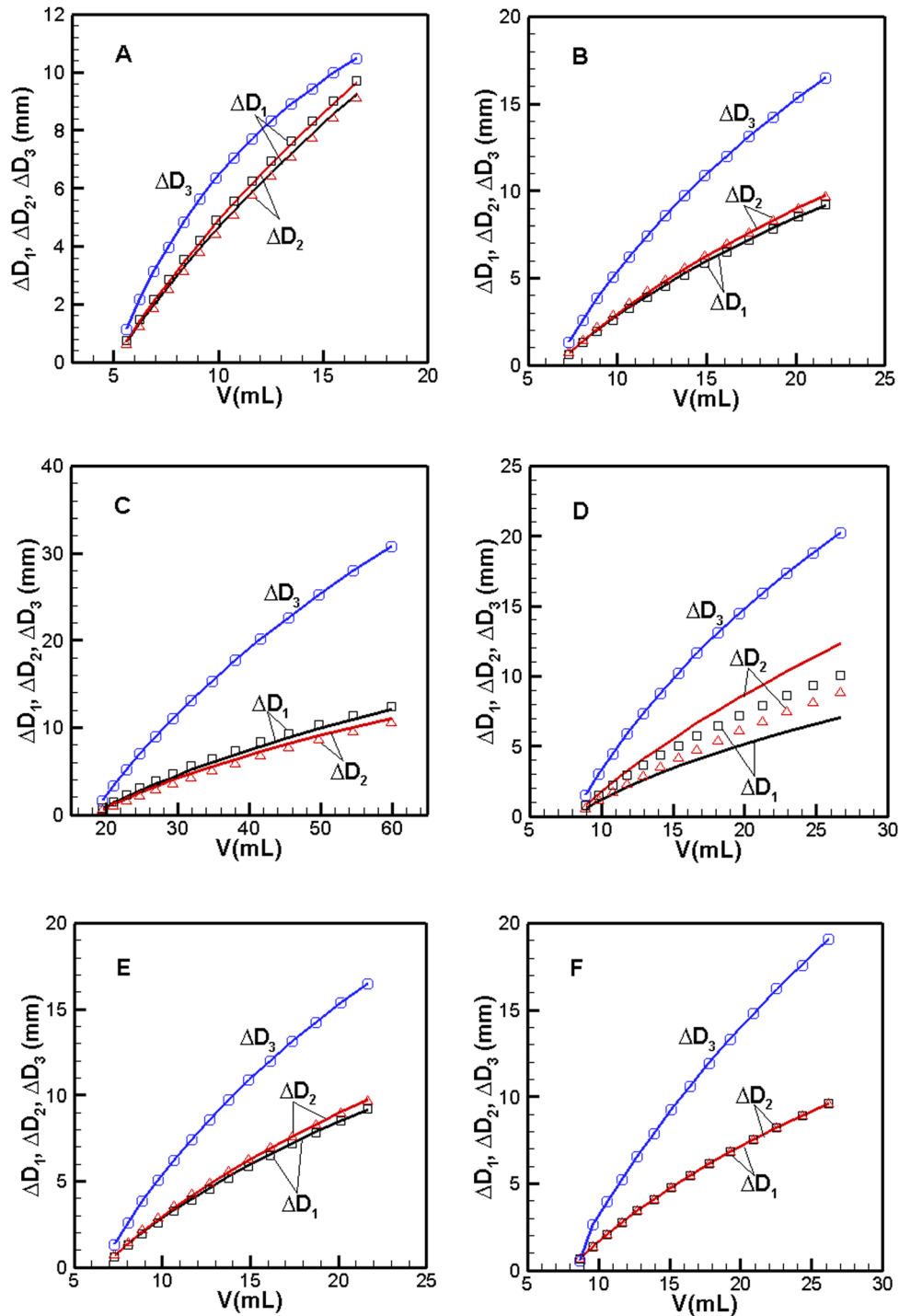
Fig. 8 Comparison of the peak displacements along the three axes of the 6 GB models between the images and computed results. The solid lines are the computed values, and the symbols are from images. Note the computed ΔD_i ($i = 1,2$) agree automatically with ΔD_i^{exp} for all samples except GB-D.

mean compliance based on an ex vivo experiment carried out by our group.

We measured the compliances of four GB samples freshly removed from patients. These GBs were stimulated with a certain amount of CCK, followed by saline infusion. The pressure and saline volume were recorded to give the pressure-volume curves. Figure 10(a) shows the compliances of these GBs estimated from these measurements. The average value of $C = 2.73$ mL/mmHg agrees well with the experimental data, as well as with in vivo observation by Middelfart et al. [38]. We note in particular that the

agreement improves as volume increases. Although in this particular study, an averaged value of compliance is used for all samples to estimate the pressure, which somewhat limits the impact of the work, the model could be used with greater accuracy if a database of human GB compliance can be established in future that is more patient-customised with gender, age, blood pressure, and GB wall thickness.

The peak stresses in the GB wall are believed to correlate strongly with GB pain [6–8]. It is therefore important to estimate these stresses in vivo noninvasively from clinical images, and
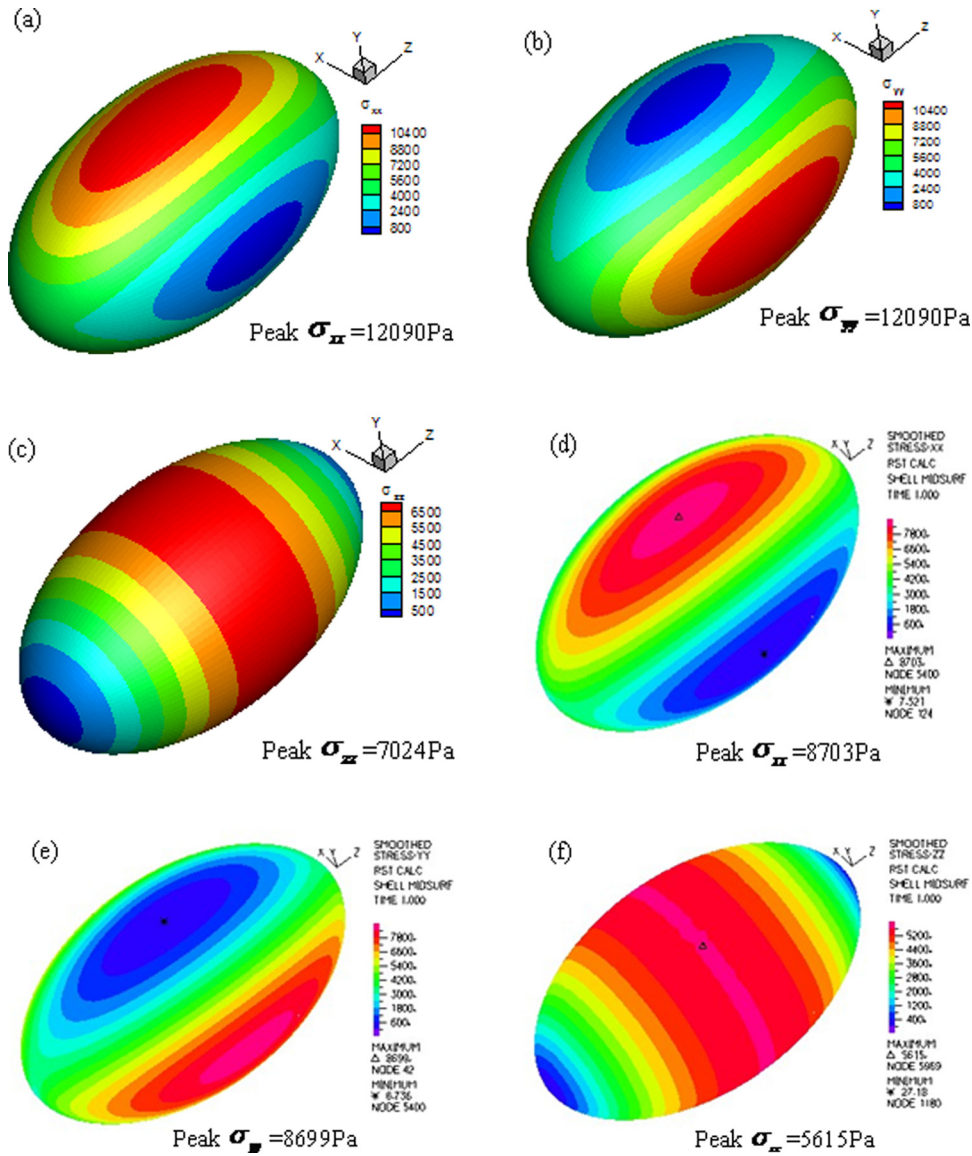
Fig. 9 Comparison of the stress component distributions between the linear membrane solution of the linear membrane model (Li et al. [7]) and the present approach for GB-F at the beginning of emptying, (a)–(c) linear membrane, (d)–(f) present results

Table 3 Comparison of the peak principal stresses at the beginning of emptying

GB	σ_1(Pa)			σ_2(Pa)		
	Linear model	Present approach	Ratio	Linear model	Present approach	Ratio
A	9170	7018	1.31	7907	5381	1.47
B	10582	7569	1.40	6001	5049	1.19
C	23265	19126	1.22	16951	14053	1.21
D	23733	9196	2.58	13934	7158	1.95
E	14478	13687	1.06	13578	8370	1.62
F	12093	8728	1.39	7204	5546	1.20

with minimum assumptions. This work investigates a quasi-nonlinear method in which the anisotropic elastic moduli are inversely estimated, and the stresses evaluated accordingly. The estimated deformation also agrees excellently with the images of the GB. The estimated incremental elastic moduli are found to be strongly patient-specific. This would affect the strain/stresses experienced in the GB wall even under the same loading pressure.

Importantly, although the estimated stresses from the present model differ somewhat from that of the linear membrane model [7], the general trend predicted is similar. In particular, GB samples with much higher first principal stress σ_1 (GB-C, GB-B, GB-D) are those associated with the patients who experienced GB pain. This agrees with our earlier finding using the linear membrane model [7].
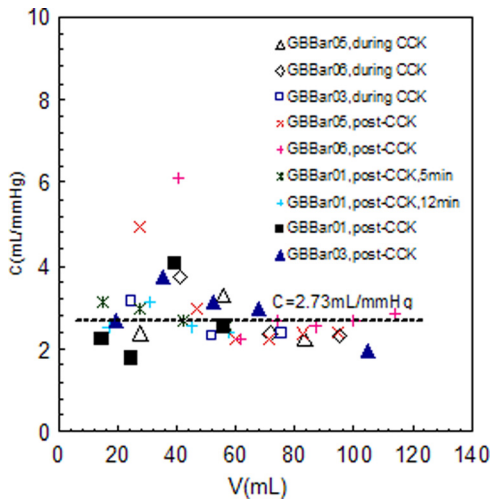
Fig. 10 In vitro measurement of GB compliance for four different samples, during and post CCK applications, with a mean value of $C = 2.73$ mL/mmHg (dotted line)

An exponential stress-strain relation similar to Eq. (6) has been established in many soft tissues in their passive state; examples are the porcine common bile duct [39,40], rat small intestine [41,42], rat and rabbit stomach [43], bladder [44], and cat/canine heart muscle [45,46]. However, it is difficult to directly compare our estimated elastic moduli with published data. The value of the passive Young's moduli of the guinea-pig GB have been found to be between 11 kPa and 88 kPa, and the fitted σ–ε curve (under $[ACh] = 10^{-4}$M) for the experimental data is $\sigma = 13.825 \exp(6.6375\varepsilon)$ kPa [47]. The parameters seem to be somewhat higher than those from our model (Table 2). This could be due to the inter-species differences between human and guinea-pig GB.

At the beginning of the GB emptying, the ratio of the active stress to the passive stress is found to be between 0.2 and 0.6 for human GBs, and it gradually drops off to zero as the emptying progresses. A similar ratio ($\sim$0.4) is found in the descending thoracic aortic wall of dog by Barra et al. [48]. Importantly, Barra et al. [48] also reported that the total, active and passive stresses all fit well with an exponential function in the form of Eq. (6).

In addition to the quasi-linear assumption, the other limitation of the present analysis is that we assume that GB wall is homogeneous and transversely isotropic. It has been shown that the response of the strips cut from a GB neck is significantly smaller than that from the GB body [2], suggesting that the elastic modulus might vary along the longitudinal direction as well. An interesting study concerning vascular soft tissue with different local Young's moduli was carried out by Khalil et al. [49]. How to model such a complicated material is a current research challenge.

We further mention that the biomechanical model of the GB wall proposed here is only applicable to GB samples that deform as ellipsoids of revolution. However, in general, not all GB shapes preserve the cross-sectional symmetry. It is for this reason that the inverse tracking of the geometries for GB-D leads to noticeable discrepancies along the two short axes (see Fig. 8). More sophisticated anisotropic constitutive modeling is required to extend our work to general ellipsoid shapes which are observed in many GB samples.

Our model is based on the assumption that the GB shape is ellipsoidal. While this is a clinically accepted assumption, it has been pointed out that the error between the actual image and an ellipsoid assumption is around 12.5% [50]. The error in the stress estimation from more realistic geometries of GB needs to be addressed in the future.

Finally, we comment that like all soft tissues, GB wall presents viscoelastic behavior [3], which means that refilling and emptying follow different loading paths. This should also be addressed in the future.

5 Conclusions

A quasi-nonlinear approach was proposed to estimate the mechanical properties of the human GB wall based on ultrasound images. The approach is built on an incremental linear material model by inversely tracking the elastic moduli in the circumferential and longitudinal directions between two successive pressure loadings. The analysis was performed on six human GB samples using ellipsoid models, and the results demonstrated that the human GB walls are circumferentially stiffer and hence anisotropic. The advantage of the quasi-nonlinear analysis is that it is easy to match the GB images and to reach converged solutions in the inverse approach. The stresses estimated by the present analysis are also consistent with those from an earlier linear membrane model. The estimated elastic moduli are found to be patient-specific, and the principal stress-strain curve can be fitted well with an exponential function, which is representative of behavior of other soft tissues observed in the literature.

References

[1] Caldwell, F. T., Jr., Sherman, E. B., and Levitsky, K., 1969, "The Composition of Bladder Bile and the Histological Pattern of the Gallbladder and Liver of the Sea Cow," Comp. Biochem. Physiol., **28**(1), pp. 437–440.

[2] Bird, N., Wegstapel, H., Chess-Williams, R., and Johnson, A. G., 1996, "In Vitro Contractility of Simulated Human and Non-Stimulated Gallbladder Muscle," Neurogastroenterol. Motil., **8**(1), pp. 63–68.

[3] Su, Y., 2005, "The Mechanical Properties of Human Gallbladder," Ph.D. thesis, Department of Mechanical Engineering, University of Sheffield, Sheffield, UK.

[4] Bertuzzi, A., Gandolfi, A., Greco, A. V., Mancinelli, R., Mingrone, G., and Salinari, S., 1992, Material Identification of Guinea-Pig Gallbladder Wall, 14th Annual International Conference of the IEEE, Engineering in Medicine and Biology Society.

[5] Liao, D., Duch, B., Stødkilde-Jørgensen, H., Zeng, Y., Gregersen, H., and Kassab, G., 2004, "Tension and Stress Calculations in a 3-D Fourier Model of Gall Bladder Geometry Obtained From MR Images," Ann. Biomed. Eng., **32**(5), pp. 744–755.

[6] Li, W., Luo, X., Hill, N., Smythe, A., Chin, S., Johnson, A., and Bird, N., 2008, "Correlation of Mechanical Factors and Gallbladder Pain," Comput. Math. Methods Med., **9**(1), pp. 27–45.

[7] Li, W. G., Luo, X. Y., Hill, N. A., Ogden, R. W., Smythe, A., Majeed, A., and Bird, N., 2011, "A Mechanical Model for CCK-Induced Acalculous Gallbladder Pain," Ann. Biomed. Eng., **39**(2), pp. 786–800.

[8] Li, W., Luo, X., Hill, N., Ogden, R., Tian, T., Smythe, A., Majeed, A., and Bird, N., 2011, "Cross-Bridge Apparent Rate Constants of Human Gallbladder Smooth Muscle," J. Muscle Res. Cell Motil., **32**(3), pp. 209–220.

[9] Tilleman, T. R., Tilleman, M. M., and Neumann, M., 2004, "The Elastic Properties of Cancerous Skin: Poisson's Ratio and Young's Modulus," Isr. Med. Assoc. J., **6**(12), pp. 753–755. Available at: http://www.ima.org.il/imaj/ar04dec-8.pdf.

[10] Schulze-Bauer, C. A., and Holzapfel, G. A., 2003, "Determination of Constitutive Equations for Human Arteries From Clinical Data," J. Biomech., **36**(2), pp. 165–169.

[11] Karimi, R., Zhu, T., Bouma, B. E., and Kaazempur Mofrad, M. R., 2008, "Estimation of Nonlinear Mechanical Properties of Vascular Tissues via Elastography," Cardiovasc. Eng., **8**(4), pp. 191–202.

[12] Escoffier, C., de Rigal, J., Rochefort, A., Vasselet, R., Lévêque, J. L., and Agache, P. G., 1989, "Age-Related Mechanical Properties of Human Skin: An In Vivo Study," J. Invest. Dermatol., **93**(3), pp. 353–357.

[13] Lee, T., Garlapati, R. R., Lam, K., Lee, P. V., Chung, Y. S., Choi, J. B., Vincent, T. B., and Das De, S., 2010, "Fast Tool for Evaluation of Iliac Crest Tissue Elastic Properties Using the Reduced-Basis Methods," Biomech. Eng., **132**, p. 121009.

[14] Samani, A., and Plewes, D., 2007, "An Inverse Problem Solution for Measuring the Elastic Modulus of Intact Ex Vivo Breast Tissue Tumours," Phys. Med. Biol., **52**, pp. 1247–1257.

[15] Iding, R. H., Pister, K. S., and Taylor, R. L., 1974, "Identification of Nonlinear Elastic Solids by a Finite Element Method," Comput. Methods Appl. Mech. Eng., **4**(2), pp. 121–142.

[16] Govindjee, S., and Mihalic, P. A., 1996, "Computational Methods for Inverse Finite Elastostatics," Comput. Methods Appl. Mech. Eng., **136**(1–2), pp. 47–57.

[17] Govindjee, S., and Mihalic, P. A., 1998, "Computational Methods for Inverse Deformations In Quasi Incompressible Finite Elasticity," Int. J. Numer. Methods Eng., **43**(5), pp. 821–838.

[18] Lu, J., Zhou, X., and Raghavan, M. L., 2007, "Computational Method of Inverse Elastostatics for Anisotropic Hyperelastic Solids," Int. J. Numer. Methods Eng., **69**(6), pp. 1239–1261.

[19] Lu, J., Zhou, X., and Raghavan, M. L., 2007, "Inverse Elastostatic Stress Analysis in Pre-Deformed Biological Structures: Demonstration Using Abdominal Aortic Aneurysms," J. Biomech., **40**(3), pp. 693–696.

[20] Lu, J., Zhou, X., and Raghavan, M. L., 2008, "Inverse Method of Stress Analysis for Cerebral Aneurysms," Biomech. Model. Mechanbiol., **7**(6), pp. 477–486.

[21] Gee, M., Reeps, C., Eckstein, H., and Wall, W., 2009, "Prestressing in Finite Deformation Abdominal Aortic Aneurysm Simulation," J. Biomech., **42**(11), pp. 1732–1739.

[22] Zhou, X., Raghavan, M. L., Harbaugh, R. E., and Lu, J., 2010, "Patient-Specific Wall Stress Analysis in Cerebral Aneurysms using Inverse Shell Model," Ann. Biomed. Eng., **38**(2), pp. 478–489.

[23] Guo, Z., You, S., Wan, X., and Bicanic, N., 2010, "A FEM-Based Direct Method for Material Reconstruction Inverse Problem in Soft Tissue Elastography," Comput. Struct., **88**(23–24), pp. 1459–1468.

[24] Raghupathy, R., and Barocas, V. H., 2010, "Generalized Anisotropic Inverse Mechanics for Soft Tissues," Biomech. Eng., **132**, p. 081006.

[25] Moulton, M. J., Creswell, L. L., Actis, R. L., Myers, K. W., Vannier, M. W., Szabo, B. A., and Pasque, M. K., 1995, "An Inverse Approach to Determining Myocardial Material Properties," J. Biomech., **28**(8), pp. 935–948.

[26] Kauer, M., Vuskovic, V., Dual, J., Szekely, G., and Bajka, M., 2002, "Inverse Finite Element Characterization of Soft Tissues," Med. Image Anal., **6**(3), pp. 275–287.

[27] Seshaiyer, P., and Humphrey, J. D., 2003, "A Sub-Domain Inverse Finite Element Characterization of Hyperelastic Membranes Including Soft Tissues," J. Biomech. Eng., **125**, pp. 363–371.

[28] Bosisio, M., Talmant, M., Skalli, W., Laugier, P., and Mitton, D., 2007, "Apparent Young's Modulus of Human Radius Using Inverse Finite-Element Method," J. Biomech., **40**(9), pp. 2022–2028.

[29] Lei, F., and Szeri, A., 2007, "Inverse Analysis of Constitutive Models: Biological Soft Tissues," J. Biomech., **40**(4), pp. 936–940.

[30] Gokhale, N. H., Barbone, P. E., and Oberai, A. A., 2008, "Solution of the Nonlinear Elasticity Imaging Inverse Problem: The Compressible Case," Inverse Probl., **24**, p. 045010.

[31] Li, J., Cui, Y., English, R., and Noble, J. A., 2009, "Ultrasound Estimation of Breast Tissue Biomechanical Properties Using a Similarity-Based Non-Linear Optimization Approach," J. Strain Anal. Eng. Des., **44**(5), pp. 363–374.

[32] Balocco, S. Camara, O., Vivas, E., Sola, T., Guimaraens, L., van Andel, H. A., Majoie, C. B., Pozo, J. M., Bijnens, B. H., and Frangi, A. F., 2010, "Feasibility of Estimating Regional Mechanical Properties of Cerebral Aneurysms In Vivo," Med. Phys., **37**, pp. 1689–1706.

[33] Kroon, M., 2010, "A Numerical Framework for Material Characterisation of Inhomogeneous Hyperelastic Membranes by Inverse Analysis," J. Comput. Appl. Math., **234**(2), pp. 563–578.

[34] Smythe, A., Majeed A., Fitzhenry, M., and Johnson, A., 1998, "A Requiem for the Cholecystokinin Provocation Test?," Gut, **43**(4), pp. 571–574.

[35] Bergel, D., 1961, "The Static Elastic Properties of the Arterial Wall," J. Physiol., **156**(3), pp. 445–457. Available at: http://jp.physoc.org/content/156/3/445.full.pdf.

[36] Fung, Y. C., 1967, "Elasticity of Soft Tissues in Simple Elongation," Am. J. Physiol., **213**(6), pp. 1532–1544. Avaiable at: http://ajplegacy.physiology.org/content/213/6/1532.full.pdf.

[37] Wu, H. C., and Yao R. F., 1976, "Mechanical Behavior of the Human Annulus Fibrosus," J. Biomech., **9**(1), pp. IN1 3–7.

[38] Middelfart, H., Jensen, P., Højgaard, L., and Funch-Jensen, P., 1998, "Pain Patterns After Distension of the Gallbladder in Patients With Acute Cholecystitis," Scand. J. Gastroenterol., **33**(9), pp. 982–987.

[39] Duch, B. U., Andersen, H., Smith, J., Kassab, G., and Gregersen, H., 2002, "Structural and Mechanical Remodelling of the Common Bile Duct After Obstruction," Neurogastroenterol. Motil., **14**(2), pp. 111–122.

[40] Duch, B. U., Andersen, H., and Gregersen, H., 2004, "Mechanical Properties of the Porcine Bile Duct Wall," Biomed. Eng. Online, **3**(1), pp. 23–31.

[41] Dou, Y., Lu, X., Zhao, J., and Gregersen, H., 2002, "Morphometric and Biomechanical Remodelling in the Intestine After Small Bowel Resection in the Rat," Neurogastroenterol. Motil., **14**(1), pp. 43–53.

[42] Dou, Y., Fan, Y., Zhao, J., and Gregersen, H., 2006, "Longitudinal Residual Strain and Stress-Strain Relationship in Rat Small Intestine," Biomed. Eng. Online, **5**(1), pp. 37–46.

[43] Zhao, J., Liao, D., and Gregersen, H., 2005, "Tension and Stress in the Rat and Rabbit Stomach are Location-and Direction-Dependent," Neurogastroenterol. Motil., **17**(3), pp. 388–398.

[44] Colding-Jørgensen, M., and Steven, K., 1993, "A Model of the Mechanics of Smooth Muscle Reservoirs Applied to the Intestinal Bladder," Neurourol. Urodyn., **12**(1), pp. 59–79.

[45] Yeatman, L., Parmley, W. W., and Sonnenblick, E., 1969, "Effects of Temperature on Series Elasticity and Contractile Element Motion in Heart Muscle," Am. J. Physiol. Legacy Content, **217**(4), pp. 1030–1034. Available at: http://ajplegacy.physiology.org/content/217/4/1030.full.pdf.

[46] Mirsky, I., and Parmley, W. W., 1973, "Assessment of Passive Elastic Stiffness for Isolated Heart Muscle and the Intact Heart," Circ. Res., **33**(2), pp. 233–243.

[47] Washabau, R., Wang, M., Dorst, C., and Ryan, J., 1991, "Effect of Muscle Length on Isometric Stress and Myosin Light Chain Phosphorylation in Gallbladder Smooth Muscle," Am. J. Physiol., Gastrointest. Liver Physiol., **260**(6), pp. G920–G924. Available at: http://ajpgi.physiology.org/content/260/6/G920.full.pdf.

[48] Barra, J., Armentano, R., Levenson, J., Fischer, E., Pichel, R., and Simon, A., 1993, "Assessment of Smooth Muscle Contribution to Descending Thoracic Aortic Elastic Mechanics in Conscious Dogs," Circ. Res., **73**(6), pp. 1040–1050.

[49] Khalil, A. S., Bouma, B. E., and Kaazempur Mofrad, M. R., 2006, "A Combined FEM/Genetic Algorithm for Vascular Soft Tissue Elasticity Estimation," Cardiovasc. Eng., **6**(3), pp. 93–102.

[50] Pauletzki, J., Sackmann, M., Holl, J., and Paumgartner, G., 1996, "Evaluation of Gallbladder Volume and Emptying With a Novel Three-Dimensional Ultrasound System: Comparison With the Sum-Of-Cylinders and the Ellipsoid Methods," J. Clin. Ultrasound, **24**(6), pp. 277–285.